

Uncertainty in identifying contact stiffness in a dovetail attachment for turbine blades

Original

Uncertainty in identifying contact stiffness in a dovetail attachment for turbine blades / Botto, D.; Glorioso, M.; Occhipinti, S.; Cuccovillo, F.. - In: MECHANICAL SYSTEMS AND SIGNAL PROCESSING. - ISSN 0888-3270. - ELETTRONICO. - 197:(2023). [10.1016/j.ymsp.2023.110379]

Availability:

This version is available at: 11583/2978403 since: 2023-05-09T08:25:56Z

Publisher:

ACADEMIC PRESS LTD- ELSEVIER SCIENCE

Published

DOI:10.1016/j.ymsp.2023.110379

Terms of use:

This article is made available under terms and conditions as specified in the corresponding bibliographic description in the repository

Publisher copyright

Elsevier preprint/submitted version

Preprint (submitted version) of an article published in MECHANICAL SYSTEMS AND SIGNAL PROCESSING © 2023, <http://doi.org/10.1016/j.ymsp.2023.110379>

(Article begins on next page)

Uncertainty in identifying contact stiffnesses in a dovetail attachment for turbine blades

Daniele Botto^{a,*}, Matteo Glorioso^a, Serena Occhipinti^a, Federica Cuccovillo^a

^a*Department of Mechanical and Aerospace Engineering - Politecnico di Torino, 10129 Torino, Italy*

Abstract

Designing bladed disks in turbo engines requires accurate dynamic models to correctly estimate resonance frequencies and related stresses. These stresses are of fundamental importance to assess the fatigue strength of blades. The contact parameters - stiffness and damping in the blade attachments - are currently among the most significant uncertainties of such models. Dry friction and alternating relative motions between the contact interfaces determine the transition between stick and slip that causes the nonlinear behavior of attachments. As a consequence, the joint contact parameters depend on centrifugal loads and amplitude vibration of blades. Commercial and in-house finite element software make use of specific contact elements to simulate dry friction and the resulting nonlinear behavior. These elements require the friction coefficient as input while the normal and tangential contact stiffness can be directly evaluated by the software or set up by the user. Researchers have been working to evaluate the contact parameters with theoretical models or to measure them with laboratory apparatus or in the field. The main objective of the present research is to discuss the uncertainty associated with identifying with experimental data the normal and tangential stiffness in a dovetail coupling. In addition, the reliability of available theoretical contact models will be addressed. A novel experimen-

*Corresponding author

Email addresses: daniele.botto@polito.it (Daniele Botto),
matteo.glorioso@studenti.polito.it (Matteo Glorioso), serena.occhipinti@polito.it
(Serena Occhipinti), federica.cuccovillo@polito.it (Federica Cuccovillo)

tal procedure was developed to evaluate the influence of an attachment on the blade dynamics. The response of the blade/attachment system was measured as a function of the axial load (simulating the centrifugal force) and of the blade vibration amplitude. An identification procedure using a finite element model was set up to identify the normal and tangential contact stiffness of the attachment. These stiffnesses were compared with the values predicted by a theoretical model. The comparison highlights a significant difference between measured and predicted stiffness. The final discussion focuses on the significance of theoretical contact stiffness and its use in finite element models.

Keywords: Contact stiffness, Contact model, Dovetail, Turbine blade

1. Introduction

1.1. Background

Mechanical design of bladed disks in aero-engines includes the assessment of structural integrity against fatigue, be it high cycle, low cycle, or fretting fatigue [1, 2]. To correctly predict stresses due to vibrations, accurate dynamic models are necessary. A complete resonance decoupling of such components is not a viable design choice because of the high modal density of the disk and the broad spectrum of the external loads. For this reason, damping introduced by dry friction is one of the tools used to reduce the amplitude of vibration. Friction damping develops at contact surfaces between shrouds, damper and under-platforms, disk slot and blade attachment, and more generally whenever interfaces are present.

Numerical simulations of models with interfaces are challenging because the tangential force in oscillating contacts is a piecewise function depending on the state of the contact, stick, slip or even separation of the surfaces. Researchers have been working to develop efficient methods to solve the nonlinear equation of motion of dynamic systems embedding friction contacts. A new method, the harmonic balance technique, was proposed by in [3] to avoid the time domain solution of the dynamic equations of nonlinear circuits. This technique,

1
2
3
4
5
6
7
8
9
20 known as Harmonic Balance Method (HBM), was widely used to determine
10 the steady-state forced response of mechanical systems with nonlinear behavior
11 [4]. An incremental HBM method, named as Multi-Harmonic Balance Method
12 (MHBM), was developed in [5] for the analysis of damped systems with dry
13 friction. In [6] this method was enhanced using a Fast Fourier Transform algo-
14 rithm to transfer the equation of motion from time to frequency domain and
15 vice versa. Nowadays, this technique is usually employed to study the dynamic
16 behavior of bladed disks in turbomachines [7]. The method was improved with
17 an analytical formulation of the contact forces [8] or by adding the static com-
18 ponent of the contact force [9, 10]. Time integration remains the most used tool
19 to evaluate transients and even more efficient methods were put forward, see for
20 example the one proposed in [11]. The aforementioned techniques make use of
21 contact models based on Jenkins element in which the contact is composed by
22 a linear spring in series with a Coulomb slider. Contact models evolved from
23 the earlier one-dimensional [12] and two-dimensional [13] (2D) models to the
24 more complete three dimensional frictional contacts [14] with variable normal
25 load [15].

26
27
28
29
30
31
32
33
34
35
36 These models require three parameters to define the contact properties: the
37 friction coefficient μ , the tangential and the normal contact stiffness, k_t and k_n
38 respectively. The normal contact stiffness k_n for non-conforming geometries can
39 be calculated with the Hertz theory as reported in [16]. The normal contact
40 deformation of cylinders, despite their simple geometry, is a challenging task
41 and several solutions are available in the literature [17–19]. The most reliable
42 solution, supported by experimental tests, is the one proposed in [20]. The
43 Hertz theory of contact was extended to account for friction forces and calcu-
44 late the tangential stiffness between spherical bodies [21, 22]. The solution for
45 the contact of nonspherical bodies subjected to oblique loading was given in
46 [23]. Among conforming geometries the rigid punch with rounded edges has a
47 very important practical application in aero-engines because it is similar to the
48 contact between the lobes in the disk slot and in the blade root. The pressure
49 distribution was given in [24] for a friction-less rigid punch on an elastic half-
50
51
52
53
54
55
56
57
58
59
60
61
62
63
64
65

1
2
3
4
5
6
7
8
9 space, while the effect of a tangential force on the state of stress was studied
10 in [25]. The latter determined the boundary between stick and slip regions and
11 the traction distribution. The theory presented in [25] was developed for 2D
12 geometries and subsequently extended to three-dimensional (3D) contact bodies
13
14
15 in [26]. This paper presents a semi-analytical method to evaluate the tangential
55 force and displacements for a 3D punch with rounded edges. The contact
16 stiffness and the dissipated energy are determined from the hysteresis loop (the
17 friction force against the tangential displacement), provided the friction coefficient
18 is known. The contact stiffness was also evaluated in its complex form by
19
20
21
22
23
24
25
26
27
28
29 using an harmonic balance so that the imaginary part of the complex stiffness,
60 that is in phase with the velocity [27], represents the damping effect. Calculation
30 of damping induced by dry friction at blade attachments is still an open
31 issue as evidenced by recent papers found in the literature [28, 29].

32
33
34
35
36
37
38
39
40
41
42
43
44
45
46
47
48
49
50
51
52
53
54
55
56
57
58
59
60
61
62
63
64
65
66
67
68
69
70
71
72
73
74
75
76
77
78
79
80
81
82
83
84
85
86
87
88
89
90
91
92
93
94
95
96
97
98
99
100
101
102
103
104
105
106
107
108
109
110
111
112
113
114
115
116
117
118
119
120
121
122
123
124
125
126
127
128
129
130
131
132
133
134
135
136
137
138
139
140
141
142
143
144
145
146
147
148
149
150
151
152
153
154
155
156
157
158
159
160
161
162
163
164
165
166
167
168
169
170
171
172
173
174
175
176
177
178
179
180
181
182
183
184
185
186
187
188
189
190
191
192
193
194
195
196
197
198
199
200
201
202
203
204
205
206
207
208
209
210
211
212
213
214
215
216
217
218
219
220
221
222
223
224
225
226
227
228
229
230
231
232
233
234
235
236
237
238
239
240
241
242
243
244
245
246
247
248
249
250
251
252
253
254
255
256
257
258
259
260
261
262
263
264
265
266
267
268
269
270
271
272
273
274
275
276
277
278
279
280
281
282
283
284
285
286
287
288
289
290
291
292
293
294
295
296
297
298
299
300
301
302
303
304
305
306
307
308
309
310
311
312
313
314
315
316
317
318
319
320
321
322
323
324
325
326
327
328
329
330
331
332
333
334
335
336
337
338
339
340
341
342
343
344
345
346
347
348
349
350
351
352
353
354
355
356
357
358
359
360
361
362
363
364
365
366
367
368
369
370
371
372
373
374
375
376
377
378
379
380
381
382
383
384
385
386
387
388
389
390
391
392
393
394
395
396
397
398
399
400
401
402
403
404
405
406
407
408
409
410
411
412
413
414
415
416
417
418
419
420
421
422
423
424
425
426
427
428
429
430
431
432
433
434
435
436
437
438
439
440
441
442
443
444
445
446
447
448
449
450
451
452
453
454
455
456
457
458
459
460
461
462
463
464
465
466
467
468
469
470
471
472
473
474
475
476
477
478
479
480
481
482
483
484
485
486
487
488
489
490
491
492
493
494
495
496
497
498
499
500
501
502
503
504
505
506
507
508
509
510
511
512
513
514
515
516
517
518
519
520
521
522
523
524
525
526
527
528
529
530
531
532
533
534
535
536
537
538
539
540
541
542
543
544
545
546
547
548
549
550
551
552
553
554
555
556
557
558
559
560
561
562
563
564
565
566
567
568
569
570
571
572
573
574
575
576
577
578
579
580
581
582
583
584
585
586
587
588
589
590
591
592
593
594
595
596
597
598
599
600
601
602
603
604
605
606
607
608
609
610
611
612
613
614
615
616
617
618
619
620
621
622
623
624
625
626
627
628
629
630
631
632
633
634
635
636
637
638
639
640
641
642
643
644
645
646
647
648
649
650
651
652
653
654
655
656
657
658
659
660
661
662
663
664
665
666
667
668
669
670
671
672
673
674
675
676
677
678
679
680
681
682
683
684
685
686
687
688
689
690
691
692
693
694
695
696
697
698
699
700
701
702
703
704
705
706
707
708
709
710
711
712
713
714
715
716
717
718
719
720
721
722
723
724
725
726
727
728
729
730
731
732
733
734
735
736
737
738
739
740
741
742
743
744
745
746
747
748
749
750
751
752
753
754
755
756
757
758
759
760
761
762
763
764
765
766
767
768
769
770
771
772
773
774
775
776
777
778
779
780
781
782
783
784
785
786
787
788
789
790
791
792
793
794
795
796
797
798
799
800
801
802
803
804
805
806
807
808
809
810
811
812
813
814
815
816
817
818
819
820
821
822
823
824
825
826
827
828
829
830
831
832
833
834
835
836
837
838
839
840
841
842
843
844
845
846
847
848
849
850
851
852
853
854
855
856
857
858
859
860
861
862
863
864
865
866
867
868
869
870
871
872
873
874
875
876
877
878
879
880
881
882
883
884
885
886
887
888
889
890
891
892
893
894
895
896
897
898
899
900
901
902
903
904
905
906
907
908
909
910
911
912
913
914
915
916
917
918
919
920
921
922
923
924
925
926
927
928
929
930
931
932
933
934
935
936
937
938
939
940
941
942
943
944
945
946
947
948
949
950
951
952
953
954
955
956
957
958
959
960
961
962
963
964
965
966
967
968
969
970
971
972
973
974
975
976
977
978
979
980
981
982
983
984
985
986
987
988
989
990
991
992
993
994
995
996
997
998
999
1000

Specific experimental campaigns were carried out to investigate the component-
scale dynamic behavior of blades fixed with typical blade-disk joints. These cam-

1
2
3
4
5
6
7
8
9 paigns provided a useful database for the validation of numerical simulations.
10 The free response of a pulled mock-blade fixed with dovetail and fir-tree joints at
11 its two ends was obtained in [42] and [43] . Damping and resonance frequencies
12
13
14 85 were extracted as functions of the amplitude of vibration for different centrifugal
15 loads. the same test rig was used in [44] to measure the forced-response and
16 to collect a database of the frequency response with different normal contact
17 loads and varying the dynamic excitation. A similar test apparatus [45] was
18 used to measure the damping introduced by the blade-disk attachment. The
19
20
21 90 joint behavior was simulated with two different contact models, one considering
22 only macroslip conditions the other based on microslip. Results showed that the
23 macroslip model was not suitable for accurate simulations. The damping ratio
24 and the natural frequency on a simple beam with dovetail root joint was also
25 measured in [46]. The centrifugal load was applied with a loading screw pushing
26
27
28 95 on the back of the dovetail while a vibration slip table provided the dynamic
29 excitation of the whole system. The micro-slip characteristic and the tangential
30 contact stiffness were measured on the same material by using a fretting test
31 rig. The contact stiffness inferred from the dynamic test performed on the sim-
32 ple beam with dovetail was compared with the results from the fretting test.
33
34
35 100 Results showed that the tangential contact stiffness measured on the dovetail is
36 smaller than the stiffness obtained by the fretting tests. The friction coefficient
37 was measured on a fir-tree attachment in [47], but the rig used in this work did
38 not allow measuring the contact stiffness.
39
40
41
42
43

44 1.2. Objective and workflow

45
46 105 Although the elastic properties of the contact in blade attachments are of
47 great significance for engineers few works were devoted to measuring these pa-
48 rameters under dynamic conditions. The objective of the present work is to
49 evaluate the uncertainty associated to the experimental identification of the
50 contact stiffnesses k_n and k_t , along the normal and tangential direction, in a
51 dovetail attachment. Moreover, the contact stiffnesses are also evaluated with
52 110 the semi-analytical models found in the literature and compared with the ex-
53
54
55
56
57
58
59
60
61
62
63
64
65

1
2
3
4
5
6
7
8
9
10
11
12
13
14
15
16
17
18
19
20
21
22
23
24
25
26
27
28
29
30
31
32
33
34
35
36
37
38
39
40
41
42
43
44
45
46
47
48
49
50
51
52
53
54
55
56
57
58
59
60
61
62
63
64
65

perimental results. This comparison was aimed to asses if the elastic contact parameters calculated with these models are feasible as contact elements in a FE model during the design step of bladed disks. The objective is pursued by collecting the dynamic response of a mock-blade with dovetail joints, as depicted in Fig. 1, and analyzing the results with the help of a FE model. The flow chart

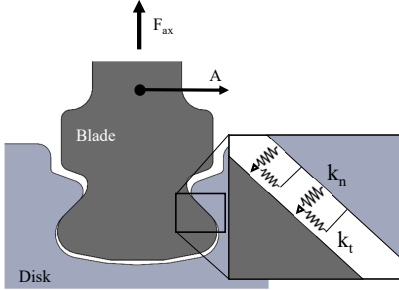


Figure 1: sketch of the dovetail joint investigated in this paper. The contact stiffnesses are highlighted in the panel.

in Fig. 2 shows the analysis procedure described in detail below.

- Section 2 reports the main findings of the method proposed in [48] to identify the instantaneous natural frequency $\omega_n(A)$ and the instantaneous damping $\eta(A)$ depending on the vibration amplitude A . More details on the method are given in [49] while properties and assumptions regarding the Hilbert transform can be found in [50]. The reader familiar with the method can skip this section.
- Section 3 describes the experimental apparatus used for the dynamic tests on the mock-blade. This apparatus utilizes the rig described in [42] but in this work a different excitation system is used. The free decay of the mock-blade is measured for different tensile axial forces F_{ax} and then processed to extract ω_n and η of the nonlinear system.
- Section 4 illustrates the FE model of mock-blade and supports. Contact elements containing the unknown stiffnesses k_t and k_n connect the corresponding contact nodes on the dovetail and on the slot. These elements

1
2
3
4
5
6
7
8
9
10
11
12
13
14
15
16
17
18
19
20
21
22
23
24
25
26
27
28
29
30
31
32
33
34
35
36
37
38
39
40
41
42
43
44
45
46
47
48
49
50
51
52
53
54
55
56
57
58
59
60
61
62
63
64
65

implement only the stick state. This section also reports the method used to obtain the reduced models of the mock-blade and supports, comprehensive of the stiffening effect due to the axial force.

- 135 • Section 5 describes how the theoretical contact stiffnesses in the attachment k_t^{th} and k_n^{th} can be calculated using the semi-analytical model of the flat punch with rounded edges proposed in [26]. The theoretical and experimental results are compared to discuss the feasibility of the theoretical model for the blade design.
- 140 • Section 6 documents the procedure to identify k_n and k_t for varying F_{ax} . The experimentally determined natural frequencies are compared with the frequencies computed by the FE model modal analysis. Appendix A reports the uncertainty of the identified stiffness.

Throughout this paper boldface letters indicate vectors and matrices. Moreover, the greek letter ω indicates frequencies in rad/s whereas f is the frequency expressed in Hz.

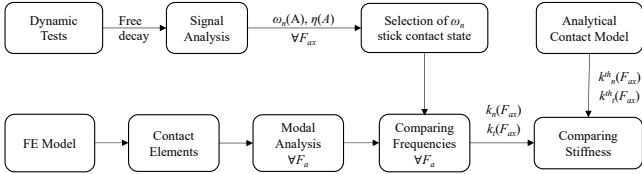


Figure 2: overview of the different phases of the activity.

2. Frequency and damping identification

The dependence of the natural frequency and damping on the amplitude of vibration, typical of nonlinear behavior, can be obtained from a free decay test with the method proposed in [48]. This method works in the time domain and is based on the analytic signal $Y(t)$ corresponding to the real signal $y(t)$

$$Y(t) = y(t) + i\tilde{y}(t) = A(t) \cdot e^{i\varphi(t)} \tag{1}$$

1
2
3
4
5
6
7
8
9 where $\tilde{y}(t)$

$$\tilde{y}(t) = H[y(t)] = \frac{1}{\pi t} * y(t) = \frac{1}{\pi} \int_{-\infty}^{+\infty} \frac{y(\tau)}{t - \tau} d\tau \quad (2)$$

10
11 is the Hilbert transform of $y(t)$. The terms $A(t)$ and $\varphi(t)$ in Eq. 1 are the
12 instantaneous amplitude and instantaneous phase of the analytic signal $Y(t)$
13 respectively.
14
15
16

17 Dry friction is the dominant source of damping in blade attachments. Friction
18 forces undergoing oscillating motion generate hysteresis loops as sketched
19 in Fig. 4b. Analysis of energy dissipation in hysteresis loops lead to the conclu-
20 sion that dry friction can be classified as a frequency-dependent damping. This
21 kind of damping is denoted to as hysteretic damping and in dynamic model it
22 is equivalent to an imaginary stiffness. The dynamic equation of motion with
23 hysteretic damping can be written as
24
25
26
27

$$m \ddot{y} + (k(A) + i h(A)) y = 0 \quad (3)$$

28
29 In Eq. 3 the stiffness $k(A)$ and the hysteretic damping $h(A)$ are unknown
30 functions and, for non linear systems, depend on the amplitude of vibration
31 A . Applying the Hilbert transform to Eq. 3 the dynamic equation of motion
32 becomes
33
34
35
36

$$m \ddot{\tilde{y}} + (k(A) + i h(A)) \tilde{y} = 0 \quad (4)$$

37
38 Multiplying each term of Eq. 4 by the imaginary unit i and adding it to the
39 corresponding term of Eq. 3 we obtain the analytic form of the equation of
40 motion
41
42
43

$$m \ddot{Y} + (k(A) + i h(A)) Y = 0 \quad (5)$$

44
45 Equation 5 can be rewritten
46
47

$$\ddot{Y} + \omega_n^2(A) (1 + i \eta(A)) Y = 0 \quad (6)$$

48
49 with
50
51

$$\omega_n^2(A) = \frac{k(A)}{m} \quad (7a)$$

$$\eta(A) = \frac{h(A)}{k(A)} \quad (7b)$$

the instantaneous natural frequency and the loss factor respectively, also referred to as modal parameters. The first and second derivative of the analytic signal in Eq. (1) are

$$\dot{Y} = \dot{y} + i\dot{\tilde{y}} = (y + i\tilde{y}) \left[\frac{\dot{A}}{A} + i\omega \right] \quad (8a)$$

$$\ddot{Y} = \ddot{y} + i\ddot{\tilde{y}} = (y + i\tilde{y}) \left[\frac{\ddot{A}}{A} - \omega^2 + i2\omega \frac{\dot{A}}{A} + i\dot{\omega} \right] \quad (8b)$$

where $\omega = \dot{\varphi}(t)$ is the instantaneous frequency of the signal. By substituting Eq. (8b) into Eq. (5) the dynamic equation of motion becomes

$$\left[\frac{\ddot{A}}{A} - \omega^2 + \omega_n^2 + i \left(2\omega \frac{\dot{A}}{A} + \dot{\omega} + \omega_n^2 \eta \right) \right] Y = 0 \quad (9)$$

By solving two equation for the real and imaginary parts of Eq. (9) we obtain the expression for the two unknown parameters

$$\omega_n^2(A) = \omega^2 - \frac{\ddot{A}}{A} \quad (10a)$$

$$\eta(A) = -\frac{1}{\omega_n^2} \left(2\omega \frac{\dot{A}}{A} + \dot{\omega} \right) \quad (10b)$$

The terms on the right-hand side of Eqs. (10) can be evaluated using the measured signal $y(t)$ and its Hilbert transform $\tilde{y}(t)$. The first derivative (Eq. 8a) gives the free vibration frequency ω and the ratio \dot{A}/A

$$\omega(t) = \frac{1}{A^2} (y\dot{\tilde{y}} - \tilde{y}\dot{y}) \quad (11a)$$

$$\frac{\dot{A}}{A}(t) = \frac{1}{A^2} (y\dot{y} + \tilde{y}\dot{\tilde{y}}) \quad (11b)$$

while the second derivative (Eq. 8b) gives the variation of free vibration frequency $\dot{\omega}$ and the ratio \ddot{A}/A

$$\dot{\omega}(t) = \frac{y\ddot{\tilde{y}} - \ddot{\tilde{y}}y}{A^2} - 2\omega \frac{\dot{A}}{A} \quad (12a)$$

$$\frac{\ddot{A}}{A}(t) = \frac{y\ddot{y} + \ddot{\tilde{y}}\tilde{y}}{A^2} + \omega^2 \quad (12b)$$

The right-hand side in Eqs. 11 and 12 depends on the Amplitude $A(t)$ that can be evaluated as

$$A(t) = \sqrt{y^2 + \tilde{y}^2} \quad (13)$$

1
2
3
4
5
6
7
8
9 **3. Experimental measurements**

10
11 *3.1. Test Rig*

12
13 Figure 3 depicts the working scheme of the test rig used in the present work.
14 The complexity of generating the centrifugal load through a rotating rig led to
15 the development of a static loading technique. The unfeasibility of statically
16 155 the development of a static loading technique. The unfeasibility of statically
17 pulling a real blade without introducing additional damping is the reason of the
18 symmetry of the rig, in which a dovetail type attachment is machined at both
19 ends of a beam with constant rectangular cross-section to create the mock-blade.
20 The equivalence of loads and joint kinematics makes the results obtained on this
21 rig comparable with those on a real disk. More detailed considerations on the
22 design principle of the rig can be found in [42].
23

24
25
26
27 The attachments are fitted into the slots machined in two supports. These
28 supports are integral with two crossbars: one crossbar is fixed while the other
29 is free to move if loaded with an axial force. The axial force F_{ax} is exerted
30 through a hydraulic cylinder operated by a manual pump. The axial force is
31 165 measured with two independent systems. A pressure gauge is connected to the
32 hydraulic cylinder and its value is read directly by the operator. A full-bridge
33 strain gauge is attached with adhesive to the mock-blade and it is read by a
34 signal conditioning card and stored by the Data AcQuisition (DAQ) system.
35
36
37
38
39
40 170 The dynamic excitation system is composed by an electrodynamic shaker and
41 its power amplifier. This amplifier is fed with a signal produced by a wave form
42 generator. The drive rod of the shaker is not fixed to the mock-blade but it
43 can be brought into contact or released by displacing the moving coil of the
44 shaker. Beforehand, the drive rod is displaced by a wave form consisting of
45 a ramp followed by a positive constant value. A proper choice of the initial
46 175 gap between the drive rod and the mock-blade together with the value of the
47 constant signal allows the drive rod to preload the mock-blade. The preload is
48 followed by a sinusoidal wave whose frequency is chosen as close as possible to
49 the resonance of the modal shape under investigation. If the preload has been
50 properly defined the drive rod remains in contact with the mock-blade during
51
52
53
54
55
56 180

1
2
3
4
5
6
7
8
9 the sinusoidal excitation period. At the end of the excitation period the drive
10 rod is suddenly detached, with a negative wave form signal, from the mock-
11 blade that from this point on is free to oscillate so that no additional damping
12 injected by the shaker. This method will be referred to as the Detached Drive
13 the
14 Rod Method (DDRM). The excitation system used in this work differs from the
15 185 one used in [42] in which the mock-blade was loaded with a non-contact exciter
16 based on electromagnets. The main objective of both systems is the same:
17 to uncouple the mock-blade from the exciter so that no additional damping is
18 injected during the free decay. With the non-contact exciter this objective is
19 achieved by stopping the current in the coil whereas with the DDRM the drive
20 190 rod is physically detached from the contact point. The main advantage of using
21 the DDRM is that the excitation force is applied at a specific point and can
22 be measured with a load cell if the forced-response is needed. The non-contact
23 exciter needs a complex calibration process to measure the transfer function
24 between the force measured on the electromagnet and the true force applied to
25 the mock-blade, as well explained in [44].

26
27
28
29
30
31 195 A Laser Doppler Vibrometer together with its controller measures the veloc-
32 ity of one reference point at time on the mock-blade. The DAQ system collects
33 and records point velocity and strain gauge signals. The wave form is created
34 with a in-house code with a sampling rate of 10 kHz and stored on file. This
35 200 file is then read by the wave form generator that provides the output voltage
36 signal.

3.2. Testing procedure

37
38
39
40
41 205 Experiments were focused on the free decay of oscillations of the first and
42 second bending mode of the mock-blade. Velocity was measured at the antinode
43 of the modal shape under investigation. For both modes a set of measurements
44 at different axial loads F_{ax} was carried out. The testing procedure for each
45 measurement is described in the following.

1. The mock-blade is pulled with the axial load F_{ax} , which is evaluated with

1
2
3
4
5
6
7
8
9
10
11
12
13
14
15
16
17
18
19
20
21
22
23
24
25
26
27
28
29
30
31
32
33
34
35
36
37
38
39
40
41
42
43
44
45
46
47
48
49
50
51
52
53
54
55
56
57
58
59
60
61
62
63
64
65

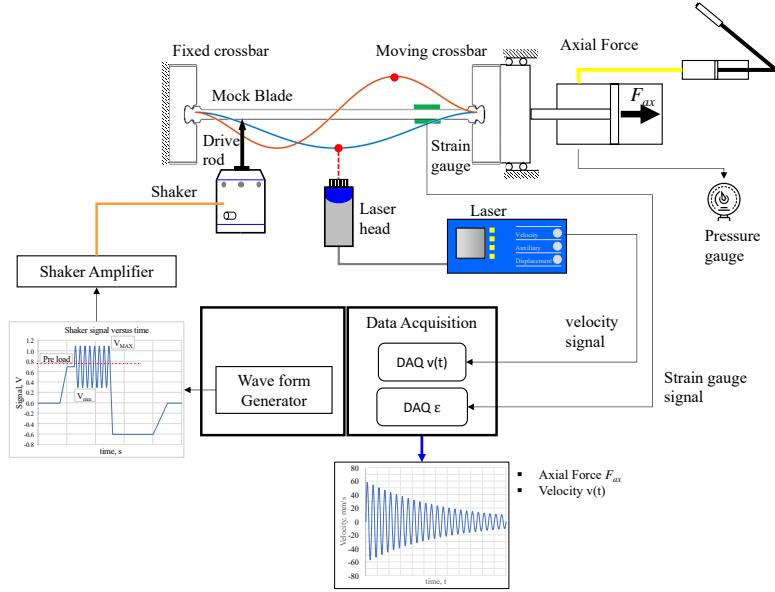


Figure 3: Test Rig scheme

the pressure gauge and strain gauges through the formulae

$$F_{ax} = A_{cyl} p \quad (14a)$$

$$F_{ax} = A_{beam} \sigma = A_{beam} E_{st} \varepsilon \quad (14b)$$

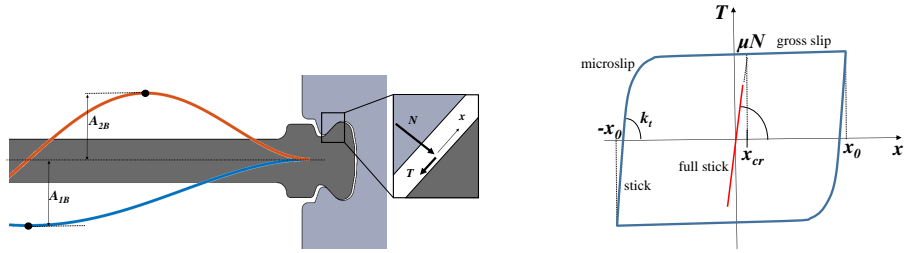
where $A_{cyl} = 1790 \text{ mm}^2$ is the effective area of the hydraulic cylinder, p is the measured pressure, $A_{beam} = 26 \times 10 \text{ mm}^2$ is the rectangular cross-section of the mock-blade, $E_{st} = 200.3 \text{ GPa}$ the Young Modulus of the blade material (steel) and ε the measured strain. The total length of the blade is 325.7mm, comprehensive of the dovetail extremities, see Fig. 9a. As reported in [42], on real engines in cruise condition a typical centrifugal load on blades is about 50 kN. The minimum load, during the flight descent phase when the engine runs at idle speed, is about 2.5 kN. In the present work measurements were performed with tensile loads up to 25 kN, a value that is representative of the real operating condition.

1
2
3
4
5
6
7
8
9
10
11
12
13
14
15
16
17
18
19
20
21
22
23
24
25
26
27
28
29
30
31
32
33
34
35
36
37
38
39
40
41
42
43
44
45
46
47
48
49
50
51
52
53
54
55
56
57
58
59
60
61
62
63
64
65

2. A preliminary hammer test is performed on the loaded mock-blade to obtain a first estimate of the natural frequencies of the first two bending modes.
3. The loaded mock-blade is excited by using the DDRM with an oscillating force whose frequency was estimated as in point 2. The free vibrations is obtained once the drive rod is detached from the excitation point.
4. The useful portion of the velocity $v(t)$ is limited to the time interval of free decay. This portion of the signal is filtered with a bandpass Parks-McClellan FIR filter, centered on the frequency of the examined mode, to reduce noise and other undesired signals.
5. The measured signal is then processed with the method described in Sect. 2. In the present work, the measured signal is the velocity $v(t) = \dot{y}(t)$. Thus, displacement $y(t)$ and acceleration $\ddot{y}(t)$ were computed by numerical integration and differentiation of $v(t)$ respectively.

3.3. Test Results

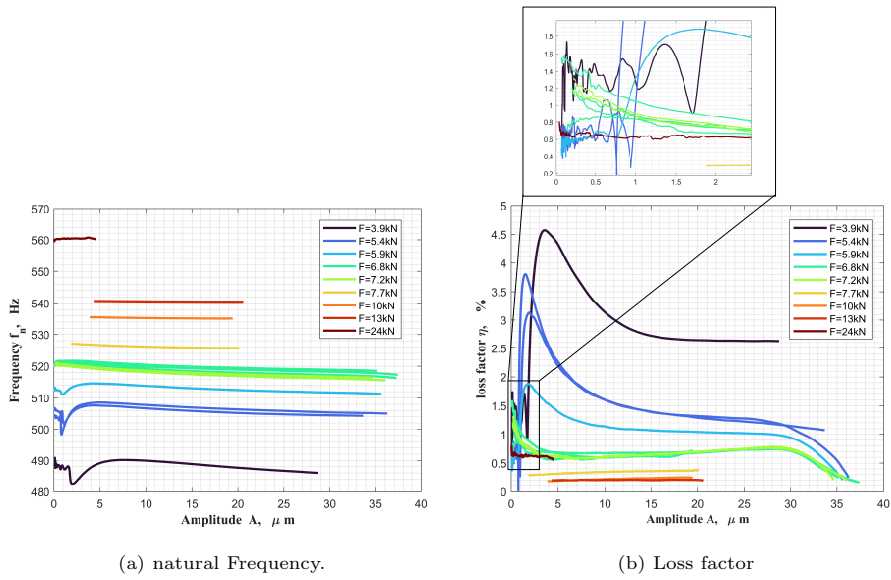
Figures 5 and 6 show the instantaneous frequency and loss factor of the first and second bending mode respectively. These dynamic parameters are evaluated with Eqs. 10. Results are shown as functions of the displacement amplitude A of the antinode. In both modes frequency and loss factor are constant for small vibration amplitudes, see the detail in Fig. 5b, thus revealing a linear behavior of the system. For small amplitudes slip is negligible whereas slip occurs for higher amplitudes. The loss factor shows a maximum, clearly visible in Fig. 5b, at an optimal amplitude A_{opt} : before A_{opt} the loss factor increases whereas after A_{opt} it decreases. This maximum is not visible for the second mode, Fig. 6b, because the output force available at the shaker was not able to displace the second mode up to the optimal amplitude. Oscillating displacements under slip condition lead to the formation of hysteresis loops as shown in Fig. 4b. Friction at interfaces dissipates energy, the amount of which is related to the loop area that varies with the amplitude A . The maximum loss factor is found at the optimal amplitude that is not the maximum amplitude.



(a) First (1B) and second (2B) Bending modes of the mock-blade. A_{1B} and A_{2B} are the displacement amplitude of their respective antinodes. In the detail the tangential T and normal N contact force and the relative displacement x at interfaces.

(b) Scheme of the Hysteresis loop between tangential force T and relative displacement x at contact interfaces. N : normal load; x_0 : maximum amplitude of vibrating displacement x ; k_t : contact tangential stiffness.

Figure 4



(a) natural Frequency.

(b) Loss factor

Figure 5: modal parameters for the first bending mode (1B).

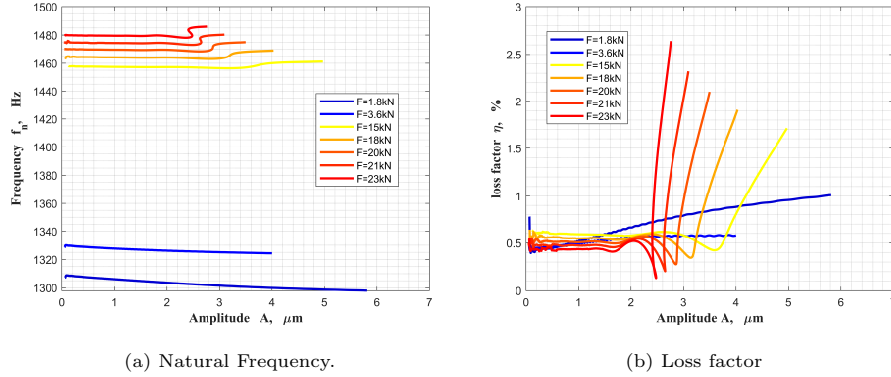
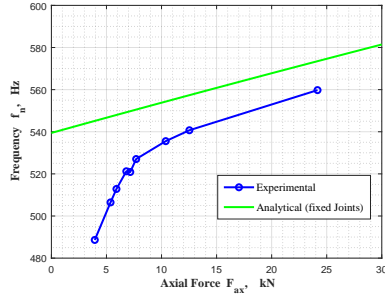


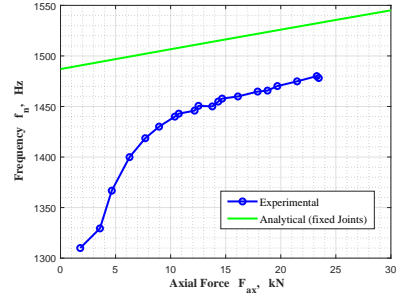
Figure 6: modal parameters for the second bending mode (2B).

The loss factor, see Figs. 5b and 6b, decreases with increasing axial loads F_{ax} , provided the amplitude is the same. This behavior is due to the increasing contact normal load N which reduces the gross-slip displacement range in the hysteresis loop, thus decreasing the dissipated energy. The natural frequency increases with axial loads F_{ax} , as reported in Figs. 5a and 6a. This increment is caused by two factors. First, the axial stress along the beam produces a moment opposing the bending deformation. This effect was considered with an analytical model [51] in which the Euler-Bernoulli beam model was modified to introduce a second order deformation effects. The effect of F_{ax} on the frequencies, evaluated with this analytical model, is depicted in Fig. 7. The second effect is related to the increasing contact normal load N that increases the stiffness of the contacts. This phenomenon will be further discussed in Sect. 6. Figure 7 also shows the natural frequencies measured in stick condition, taken as the mean value in the small amplitudes range. The measured frequency is lower than the predicted because the contact stiffness at the interfaces is in series with the mock-blade stiffness and then reduces the global stiffness. For axial loads greater than 12 kN the frequencies increase with a slope slightly higher than that predicted by the analytical model. For axial loads lower than 12 kN the experimental frequencies diverge from the theoretical ones because the interface tends to slip and the contact stiffness decreases, thus reducing the natural frequency of the

entire system.



(a) Natural frequency of the first bending mode.



(b) Natural frequency of the second bending mode.

Figure 7: stiffening effect due to the axial load F_{ax} . The increase of the frequency predicted by the analytical model is compared with the experimental results.

270 4. Finite Element model

A commercial Finite Element (FE) model was used in the procedure to identify the normal and tangential contact stiffnesses. The mock-blade and the slots, depicted in Fig. 8, were modeled as separate bodies. The material properties of the mock-blade were evaluated with a hammer modal test in free-free condition. The measured modulus of elasticity and density were $E = 200.3$ GPa and $\rho = 7592 \text{ kg/m}^3$ respectively. The contact surface on the root blade and the matching surface on the slot were discretized with the same number of nodes. These nodes have coincident coordinates, see the detail in Fig. 8, so that node-to-node contact element is allowed. These contact elements are assembled during the identification procedure.

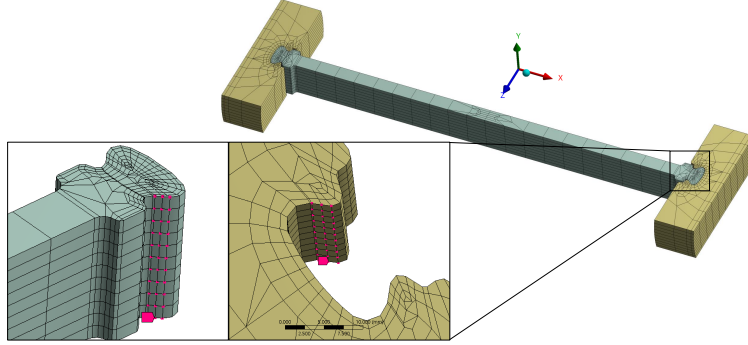


Figure 8: Finite Element model and detail of contact nodes.

4.1. Tensile force stiffening effect

The stiffening effect induced by the axial load F_{ax} was considered introducing the so-called geometrical stiffness matrix $\Delta\mathbf{K}_G$

$$\mathbf{K} = \mathbf{K}_0 + \Delta\mathbf{K}_{G,F_{ax}} \quad (15)$$

This matrix depends on the state of stress in the beam, and it was evaluated through a FE preliminary static analysis of the mock-blade for each F_{ax} applied in the experiments

$$\Delta\mathbf{K}_{G,F_{ax}} = \int_V \mathbf{S}_g^T \boldsymbol{\sigma} \mathbf{S}_g dV \quad (16)$$

In Eq. 16 \mathbf{S}_g is the matrix of the shape functions derivatives while $\boldsymbol{\sigma}$ is the stress state matrix. The stress stiffening effect is only significant in slender bodies, then it was calculated for the mock-blade but not for the supports.

The preliminary static analysis was performed by applying to the dovetails contact surfaces the normal forces N balancing the axial load F_{ax}

$$N = \frac{F_{ax}}{2 \sin \beta} \quad (17)$$

with $\beta = 45^\circ$ as sketched in Fig. 9a. Since results are little affected by contact tangential forces T these forces were neglected. The mock-blade must be properly constrained during the preliminary analysis to avoid kinematic indeterminacy that would not allow solving the static problem. Since these constraints

1
2
3
4
5
6
7
8
9
10
11
12
13
14
15
16
17
18
19
20
21
22
23
24
25
26
27
28
29
30
31
32
33
34
35
36
37
38
39
40
41
42
43
44
45
46
47
48
49
50
51
52
53
54
55
56
57
58
59
60
61
62
63
64
65

are embedded in the stiffness matrix in Eq. 15 they could invalidate the identification procedure of k_n and k_t . To avoid this issue the FE model was constrained with node-to-ground elastic springs with a very small stiffness $k = 1 \cdot 10^{-4}$ N/mm so that they have no effect on the mock-blade dynamics in the frequency range of interest. Three nodes for each dovetail were constrained along the transverse directions, see Fig. 9b, while the center node of the mock-blade was constrained along the axial direction as in Fig. 9c. The rigid motion of the mock-blade is canceled with a minimum number of constraints and complying with the symmetry of the first two modal shapes.

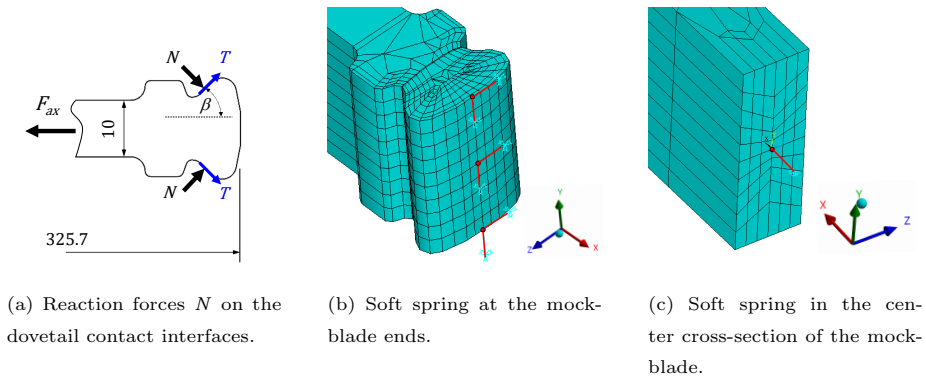


Figure 9: boundary conditions for the preliminary FE static analysis of the mock-blade.

4.2. CMS reduction

The identification of the contact stiffness was performed with a purposely developed in-house code. This code utilizes the stiffness and mass matrix generated by the FE commercial software. To decrease the computational cost and speed up the identification process the Degrees of Freedom (DoF) of the models were reduced using the tool built in the FE software. Then the reduced matrices were exported in a suitable format and read by the in-house code. The reduction was performed with the Component Mode Synthesis (CMS), a technique developed in [52] for sub-structuring, and summarized in the following. The dynamic equations in physical coordinates \mathbf{u} is

$$\mathbf{M}\ddot{\mathbf{u}} + \mathbf{K}\mathbf{u} = \mathbf{0} \tag{18}$$

The physical DoFs are divided in active \mathbf{u}_a and omitted \mathbf{u}_o

$$\mathbf{u} = \begin{Bmatrix} \mathbf{u}_a \\ \mathbf{u}_o \end{Bmatrix} \quad (19)$$

so that Eq. 18 can be rearranged as

$$\begin{bmatrix} \mathbf{M}_{aa} & \mathbf{M}_{ao} \\ \mathbf{M}_{oa} & \mathbf{M}_{oo} \end{bmatrix} \begin{Bmatrix} \ddot{\mathbf{u}}_a \\ \ddot{\mathbf{u}}_o \end{Bmatrix} + \begin{bmatrix} \mathbf{K}_{aa} & \mathbf{K}_{ao} \\ \mathbf{K}_{oa} & \mathbf{K}_{oo} \end{bmatrix} \begin{Bmatrix} \mathbf{u}_a \\ \mathbf{u}_o \end{Bmatrix} = \mathbf{0} \quad (20)$$

According to the CMS method, only the physical displacement \mathbf{u}_a of the active nodes are retained in the equation. The omitted DoFs are approximated with a linear combination of the active DoFs and normal modes Φ_{oo}

$$\mathbf{u} = \begin{Bmatrix} \mathbf{u}_m \\ \mathbf{u}_s \end{Bmatrix} = \begin{bmatrix} \mathbf{I} & \mathbf{0} \\ \mathbf{K}_{oo}^{-1}\mathbf{K}_{oa} & \overline{\Phi}_{oo} \end{bmatrix} \begin{Bmatrix} \mathbf{u}_a \\ \boldsymbol{\eta}_o \end{Bmatrix} = \mathbf{T}\mathbf{q} \quad (21)$$

The normal modes Φ_{oo} are solution to the eigenproblem of the sub-system composed of the omitted DoFs with proper boundary conditions. $\overline{\Phi}_{oo}$ is a subset of Φ_{oo} while $\boldsymbol{\eta}_o$ are the modal DoFs. The number of active and modal DoFs defines the degree of reduction. The dynamic equation 18 becomes

$$\overline{\mathbf{M}}\ddot{\mathbf{q}} + \overline{\mathbf{K}}\mathbf{q} = \mathbf{0} \quad (22)$$

with \mathbf{q} generalized DoFs and

$$\overline{\mathbf{K}} = \mathbf{T}^T \mathbf{K} \mathbf{T} \quad (23a)$$

$$\overline{\mathbf{M}} = \mathbf{T}^T \mathbf{M} \mathbf{T} \quad (23b)$$

are the reduced stiffness and mass matrices. The reduction was performed separately for the mock-blade and the two supports. The mock-blade stiffness matrix is actually a set of matrices, one for each axial load F_{ax} , according to what reported in Sect. 4.1. The active nodes on the mock-blade comprise 33 nodes on each contact interface and two line of 21 nodes each along the axial direction. These nodes allow visualizing the modal shapes during post processing of the results. One of these latter nodes coincides with the spot on which the velocity is measured, another one with the excitation point. The

subset $\bar{\Phi}_{oo}$ is composed by the first 100 modal shapes (corresponding to the lowest frequencies) which brings the total number of generalized DoFs to 622. The active nodes on the support are the nodes on the contact interfaces and 117 nodes on the base. The latter nodes allow a static analysis of the reduced model of the support. This analysis was not performed in the present work and these DoFs were constrained. Also for the support 100 modal shapes were chosen so that the number of generalized DoFs amounts to 322.

4.3. Contact element

The mock-blade roots and the supports are connected by node-to-node contact elements, namely springs acting along the normal and tangential directions of the contact surface. The stiffness of these nodal springs \tilde{k}_n and \tilde{k}_t are obtained by uniformly distributing the contact stiffness of the attachment k_n and k_t on the nodes of each interface. The contact element and its stiffness matrix and DoFs in the Local coordinate system are visible in Fig. 10.

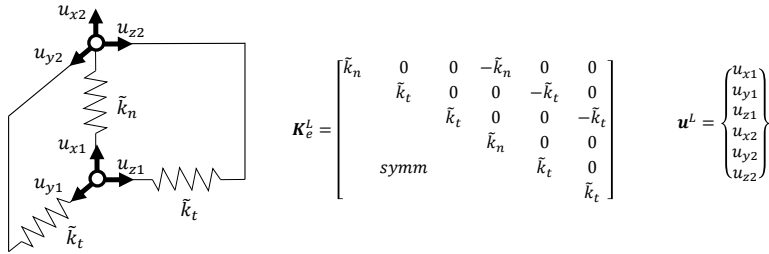


Figure 10: node-to-node contact element. \tilde{k}_n and \tilde{k}_t are the nodal stiffnesses.

5. Semi-analytical contact model

The unknown contact stiffnesses k_n and k_t were identified following the procedure described in Sect. 6. Nevertheless, the contact stiffness can be also estimated by using the semi-analytical solution of the contact between a flat punch on an infinite half-plane, as shown in Fig. 11a. These stiffnesses are referred to as theoretical contact stiffnesses k_n^{th} and k_t^{th} . The pressure distribution

1
2
3
4
5
6
7
8
9 p on a punch with rounded edges

$$\frac{bp(\phi)}{P} = \frac{2/\pi}{\pi - 2\phi_0 - \sin 2\phi_0} \left[(\pi - 2\phi_0) \cos \phi + \sin \phi \ln \left| \frac{\sin(\phi + \phi_0)}{\sin(\phi - \phi_0)} \right| + \sin \phi_0 \ln \left| \tan \frac{\phi + \phi_0}{2} \tan \frac{\phi - \phi_0}{2} \right| \right] \quad (24)$$

10
11 was first found in [24] and also recalculated in [25]. Equation 24 is given in
12 dimensionless form in which b is the contact half-width and P the normal load
13 per unit length. Figure 11a sketches the analogy between the punch geometry
14 and the contact region in the attachment. The auxiliary angle ϕ is defined as
15 $\sin \phi = x/b$ and the angle ϕ_0 implicitly specifies the half-width $b = a/\sin \phi_0$.
16 The angle ϕ_0 can be found by solving the equation

$$\frac{nPR}{a^2 E^*} = \frac{\pi - 2\phi_0}{2 \sin^2 \phi_0} - \cot \phi_0 \quad (25)$$

17 where $2a = 2.57$ mm and $1/E^* = \sum_{i=1,2} (1 - \nu_i^2)/E_i$ with $E_i = 200.3$ GPa
18 and $\nu_i = 0.3$ the Young's modulus and the Poisson's ratio of the i -body. The
19 contact length is $L=26$ mm while the curvature radius of the rounded edges
20 is $R=2.50$ mm (considering a symmetrical punch geometry). Because the real
21 profile is not symmetric R was chosen as the maximum between the two radius
22 (1.25 and 2.50 mm) corresponding to the higher values of the contact stiffnesses
23 k_n^{th} and k_t^{th} . However, the variation of the theoretical contact stiffness with the
24 radius R in the above-mentioned range is negligible.

25
26
27
28
29
30
31
32
33
34
35
36
37
38
39
40
41
42
43
44
45
46
47
48
49
50
51
52
53
54
55
56
57
58
59
60
61
62
63
64
65
330 A discrepancy was found about the coefficient n in Eq. 25: according to
[24] $n=2$ whereas [25] reports a coefficient $n=4$. Figure 11b shows the pressure
distribution calculated with the two different coefficients and compares it with
the results of a FE analysis. The coefficient $n=4$ overestimate the contact half-
width and coherently underestimate the pressure peak. For this reason, this
335 work utilizes the formulation proposed in [24].

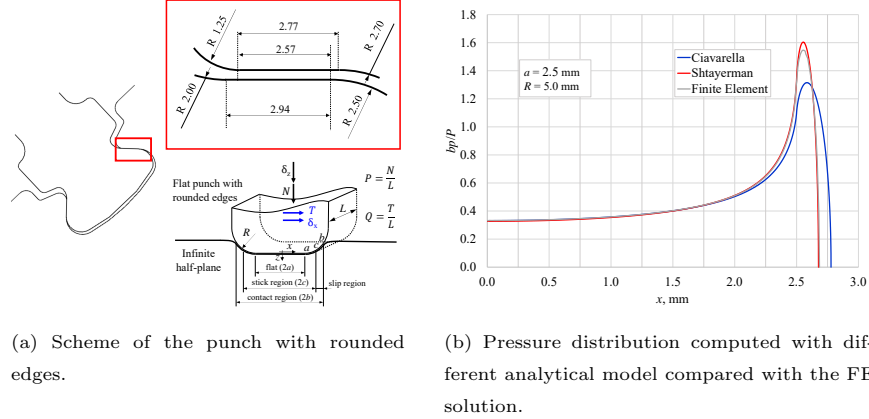


Figure 11: the punch with rounded edges and its pressure distribution.

The results obtained in [24] were extended in [25] in the case of contacts experiencing also a tangential force T . The shear stress was calculated as the sum of the stress in full slip condition $\mu p(x)$ (μ being the friction coefficient) and a corrective shear stress $q^*(x)$ in the stick region

$$q(x) = \mu p(x) - q^*(x) \quad (26)$$

The corrective shear stress distribution $q^*(\theta)$ is

$$\frac{cq^*(\theta)}{\mu P - Q} = -\frac{2/\pi}{\pi - 2\theta_0 - \sin 2\theta_0} \left[(\pi - 2\theta_0) \cos \theta + \sin \theta \ln \left| \frac{\sin(\theta + \theta_0)}{\sin(\theta - \theta_0)} \right| + \sin \theta_0 \ln \left| \tan \frac{\theta + \theta_0}{2} \tan \frac{\theta - \theta_0}{2} \right| \right] \quad (27)$$

where $\sin \theta = x/c$, $P = N/L$ and $Q = T/L$. The half-width of the stick region $c = a/\sin \theta_0$, see Fig. 11a, is computed solving for θ_0 in the equation

$$\frac{nPR}{a^2 E^*} \left(1 - \frac{Q}{\mu P} \right) = \frac{\pi - 2\theta_0}{2 \sin^2 \theta_0} - \cot \theta_0 \quad (28)$$

The tangential displacement δ_x was found in [26]

$$\delta_x = u_{x1} - u_{x2} = \frac{2}{\pi E^*} \left[-\int_{-b}^b q_x(r) \ln \left| \frac{r}{b} \right| dr + Q \left(\ln \left| \frac{L}{b} \right| + \frac{\nu}{1 - \nu} \right) \right] \quad (29)$$

through the elastic potential theory of Boussinesq-Cerruti as reported in [53]. Hence, the stiffness is calculated as the first derivative of the tangential force at

the onset of the tangential displacement for a given normal force N

$$k_t^{th}(N) = \left(\frac{\partial T}{\partial \delta_x} \right)_{\delta_x=0} = \frac{1}{\left(\frac{\partial \delta_x(N)}{\partial T} \right)_{T=0}} \quad (30)$$

Similarly, the normal displacement of each body is

$$|u_{z_i}| = \frac{1 - \nu_i^2}{\pi E_i} \int_{-b}^b p(r) \left(\int_{-L/2}^{L/2} \frac{1}{\sqrt{r^2 + s^2}} ds \right) dr = \frac{1 - \nu_i^2}{\pi E_i} \int_{-b}^b p(r) 2 \sinh^{-1} \left(\frac{L/2}{|r|} \right) dr \quad (31)$$

thus the relative normal displacement δ_z is

$$\delta_z = u_{z1} - u_{z2} = \frac{2}{\pi E^*} \int_{-b}^b p(r) \sinh^{-1} \left(\frac{L/2}{|r|} \right) dr \quad (32)$$

and the normal contact stiffness can be written as

$$k_n^{th}(N) = \frac{\partial N}{\partial \delta_z} = \frac{1}{\frac{\partial \delta_z}{\partial N}} \quad (33)$$

For a given axial force F_{ax} the corresponding normal load N ranges from a minimum N_{min} (corresponding to full slip $T=\mu N$) and a maximum value N_{max} (corresponding to a friction-less contact $T=0$)

$$\frac{F_{ax}}{2(\sin \beta + \mu \cos \beta)} \leq N \leq \frac{F_{ax}}{2 \sin \beta} \quad (34)$$

as visualized in Fig. 9a, Figure 13b shows that the theoretical contact stiffness are weakly affected by the tangential force T with $\mu=0.4$.

6. Contact stiffness Identification

The unknown contact stiffnesses k_n and k_t were indirectly estimated through their influence on the natural frequencies calculated by the reduced FE model. These frequencies, calculated for both the first (1B) and second (2B) bending mode, were compared with the measured frequencies. This comparison was carried out for each axial load F_{ax} with which experiments were performed. The analysis was achieved for small vibration amplitudes in which gross slip does not occur. In this condition the frequency remains constant, as shown in Fig. 6a, and the system exhibits a linear behavior. Microslip is always present

but its influence is significant only for axial loads less than 12 kN, as reported in Fig. 7. For this reason, only results obtained with axial loads greater than 12 kN were employed in the comparison. The unknown stiffnesses k_n and k_t can be determined by solving at each axial load F_{ax} the nonlinear system

$$\begin{cases} f_{n,1B}^{FE}(k_n, k_t) - f_{n,1B}^m \\ f_{n,2B}^{FE}(k_n, k_t) - f_{n,2B}^m \end{cases} = \begin{cases} \Delta f_{n,1B} \\ \Delta f_{n,2B} \end{cases} = \begin{cases} 0 \\ 0 \end{cases} \quad (35)$$

where f_n^{FE} and f_n^m are the computed and measured natural frequencies respectively. The natural frequencies of the first bending mode as a function of the contact stiffness are shown in Fig. 12a. Equation 35 is solved by finding the locus of the minima of the residual norm $g := \|\Delta \mathbf{f}_n\|$. This locus is characterized by a minimum gradient $\|\nabla g\|$ on the level curves of the residual norm surface

$$\begin{cases} \frac{\partial}{\partial n} \|\nabla g\| = 0 \\ \frac{\partial^2}{\partial n^2} \|\nabla g\| > 0 \end{cases} \quad (36)$$

where direction \mathbf{n} defines the level curve as $\nabla g \cdot \mathbf{n} = 0$. Together with Eq. 36 a further limit is set on the value of the norm that must be less than a selected tolerance $g < toll_g$. The locus of the minima can be visualized as the path followed by a sphere free to roll on the residual norm surface. This path is visualized by the solid line marked in Fig. 12b. This locus represents the feasible solutions and is reported in Fig. 12c for different axial loads. Once the loci are defined a single solution must be selected. In this work the following three criteria were considered.

- The most intuitive criterion is to find the global minimum of $\|\Delta \mathbf{f}_n\|$ on the minima locus. The drawback of this criterion is the low accuracy with which the stiffness is determined. The errors on the stiffness, computed with the procedure described in Appendix A, is about 55% and makes this solution less reliable. The reason for this large error is that the solution $(k_n, k_t) \simeq (1, 7)$ kN/ μ m belongs to the region in which the sensitivity of the contact stiffness to the frequency variation is high, and a small

1
2
3
4
5
6
7
8
9
10
11
12
13
14
15
16
17
18
19
20
21
22
23
24
25
26
27
28
29
30
31
32
33
34
35
36
37
38
39
40
41
42
43
44
45
46
47
48
49
50
51
52
53
54
55
56
57
58
59
60
61
62
63
64
65

355 uncertainty on the measured frequencies propagates dramatically on the stiffness value.

- Uncertainty on the identified stiffness also suggests a different criterion: selecting the solution (k_n, k_t) with the minimum error (according to the procedure described in Appendix A). This solution is denoted to as the “optimal solution pair”.
- The theoretical contact stiffnesses were calculated in Sect. 5 and their values can guide the selection procedure. A third option is to choose the pair (k_n, k_t) with the minimum distance from theoretical stiffness.

360

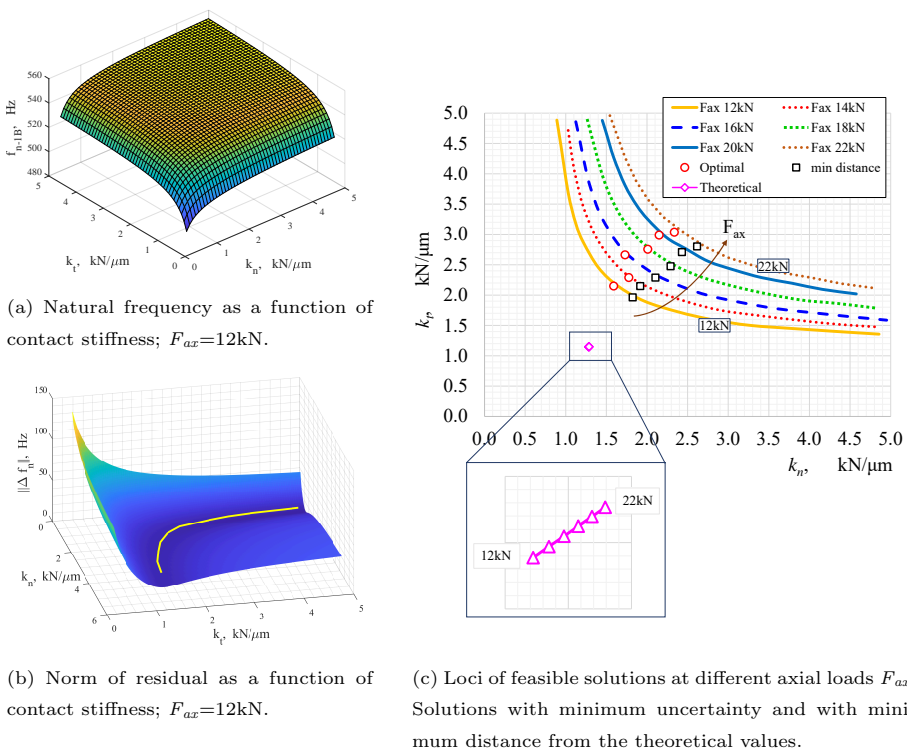


Figure 12: variation of frequency (a) and residual norm (b) with contact stiffness. Loci of the minima with optimal and minimum distance solutions for different axial loads.

Figure 12c reports the solution determined with the last two criteria: these so-

1
2
3
4
5
6
7
8
9
10
11 365 solution criterion was adopted and Table 1 reports the numerical results with
12 their accuracy. The ratio of tangential to normal stiffness remains almost con-
13 stant, $k_t/k_n \simeq 1.37$. This result differs from what reported in [54] in which this
14 ratio slowly increases with normal loading.
15

16
17
18
19 370 Figure 13a compares the optimal and the theoretical solution and points out
20 that the difference between the two results is very high. Taking the theoretical
21 stiffness as reference, the difference in the worst case is about 82% and 164% for
22 k_n and k_t respectively. Furthermore, the trend of the two solutions at varying
23 axial loads is very different. The optimal solution shows a slope of about 73
24 and 95 mm^{-1} for k_n and k_t respectively, whereas the theoretical values remains
25 almost constant at varying axial load as emphasized in Fig. 13b.
26 375
27

28
29
30
31
32
33
34
35 380 Most of this discrepancy is due to the slightly different meaning that the
36 term “contact stiffness” takes on in the numerical and analytical models. In the
37 numerical model, the optimal contact stiffness represents the local connection
38 between the two bodies through the interface that breaks off the continuum. The
39 flexibility of the bulk, here the lobes on root and slots, is considered in the finite
40 element model. The global stiffness is given by the series of the optimal and bulk
41 stiffness. On the contrary, the analytical model calculates the displacements,
42 from which the theoretical stiffness are deduced, considering the elastic half-
43 space. The comparison should be made between global and theoretical stiffness
44 rather than optimal and theoretical stiffness, but this comparison is by no means
45 an easy task.
46

47
48
49
50
51 390 Furthermore, the assumption of elastic half-space is valid only if the size $2b$ of
52 the contact region is much smaller than the curvature radius R [26], hypothesis
53 not strictly fulfilled in the real contact geometry of the examined joint.
54

55
56
57
58
59
60
61
62
63
64
65 Moreover, the blade deformation and the lobe flexibility induce rotation of
the contact surfaces. This rotation generates an asymmetric pressure distribu-
tion, whereas the theoretical model assumes that the loads and the pressure
distribution are symmetric. Since the contact problem is nonlinear asymmet-
ric pressure distributions result in different stiffness even for the same normal

load. An analytical model comprehensive of the moment and asymmetry of the contact patch was put forward in [55]. This model delivers the pressure and tangential distribution, but the displacement field from which the contact stiffness is derived is not ready yet. Furthermore, it is not easy to evaluate the moment at the root when the blade is oscillating also considering that this moment varies during a cycle.

F_{ax}	k_n	σ_{nn}/k_n	k_t	σ_{tt}/k_t
kN	kN/ μm	%	kN/ μm	%
12	1.59	15	2.15	12
14	1.68	17	2.38	15
16	1.82	21	2.57	18
18	2.01	26	2.76	22
20	2.15	27	2.99	25
22	2.34	31	3.04	26

Table 1: normal and tangential contact stiffness with their estimated errors for different axial loads.

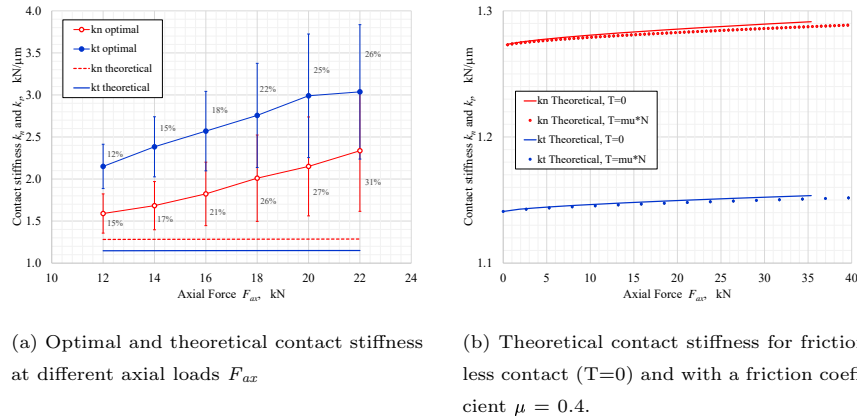


Figure 13: Comparison between the optimal contact stiffness resulting from the identification procedure and the theoretical values obtained with the semi-analytical model.

1
2
3
4
5
6
7
8
9 **7. Conclusions**

10
11 This paper has presented a novel procedure to experimentally investigate
12 normal and tangential contact stiffness in dovetail attachments. Experimental
13 data were collected on a mock-blade with a dovetail at both ends. With this
14
15
16
17 405 symmetric configuration it is possible to apply the load simulating the centrifu-
18 gal force without adding undesirable damping or stiffness. In our experiment,
19 a shaker excited the mock-blade whose free decay was measured with a laser
20 Doppler velocimeter. The Detached Drive Rod Method was developed to ensure
21 that the free decay was not affected by any coupling with the excitation system.
22
23
24 410 The measured response was transformed into an analytic signal and processed
25 to determine the instantaneous modal parameters, namely natural frequency
26 and loss factor. Results substantiate the dependency of the modal parameters
27 on the vibration amplitude, a behavior typical of nonlinear systems. Results
28 also show that the loss factor reaches a maximum at an optimal amplitude, as
29
30
31
32 415 predicted by theoretical models.

33
34 In order to determine the normal and tangential contact stiffness, part of
35 the interval of the free decay was utilized. This part of the interval was chosen
36 because the system behaves linearly and the natural frequencies are constant.
37 An FE model of the mock-blade and its supports was built within a commercial
38 software. The stiffness and mass matrices of this model were reduced using the
39
40 420 component mode synthesis method and imported in an in-house code. This
41 code identifies the contact stiffness by comparing the natural frequencies of the
42 first and second bending modes computed by the numerical model with the
43 corresponding measured frequencies. The presence of two parameters, namely
44
45
46
47 425 normal and tangential stiffness, generates a multi-objective optimization prob-
48 lem. The contact stiffness pair with minimum uncertainty was chosen among
49 the feasible solutions and named “optimal stiffness pair”. This optimal stiff-
50 ness pair was also compared with the theoretical stiffness pair calculated with
51 a semi-analytical solution. It was found that the optimal pair also minimizes
52
53
54
55 430 the distance between optimal and theoretical stiffness. The difference between
56
57
58
59
60
61
62
63
64
65

1
2
3
4
5
6
7
8
9 the optimal and theoretical results was very high, reaching 82% and 164% in
10 the worst case for k_t and k_n respectively. The trend of the contact stiffness at
11 varying axial loads was also very different. The optimal stiffness showed a slope
12 of about 73 and 95 mm⁻¹ for k_t and k_n respectively, whereas the theoretical
13 values remained almost constant.
14
15 435

16 This disagreement can be explained considering the meaning of the term
17 "contact stiffness". In the numerical model, contact stiffness represents the
18 connection between two bodies through the interface. The flexibility of the
19 bulk, represented by the lobes on the root and the slot, is considered in the fi-
20 nite element model. Instead, the theoretical model calculates the displacements
21 and then the stiffness, considering the elastic half-space. When the theoreti-
22 cal stiffnesses are assembled in the FE model it is as if the bulk flexibility is
23 considered twice.
24
25 440

26 Moreover, when contact surfaces are loaded they deform because of the flex-
27 ibility of the lobes. The pressure distribution becomes asymmetric, whereas the
28 theoretical model assumes that the loads and the pressure distribution are sym-
29 metric. Since the contact problem is nonlinear, different pressure distributions
30 result in different stiffness even if the total loads are the same. Currently, no
31 theoretical models are available which consider the moment at the interface and
32 asymmetric pressure distribution.
33
34 445

35 From the previous observations, it is clear that measured and theoretical
36 contact stiffnesses are not interchangeable. This work shows that computing
37 contact stiffnesses with a theoretical model, such as the one presented in the
38 paper, and substituting them in a finite element model underestimates the stiff-
39 ness of the whole system. Designers should be aware that in this case the modal
40 analysis and the forced response will be inaccurate.
41
42 455

43 Appendix A. Contact stiffness accuracy

44
45
46
47
48
49
50
51
52
53
54
55
56
57
58
59
60
61
62
63
64
65

Uncertainties on contact stiffness were estimated through the procedure shown in [56]. The numerical frequencies as a function of the contact stiffness

can be approximated by a first order Taylor expansion

$$\mathbf{f}(k_n, k_t) = \begin{Bmatrix} f_{n,1B}^{FE}(k_n, k_t) \\ f_{n,2B}^{FE}(k_n, k_t) \end{Bmatrix} \simeq \mathbf{f}_0 + \mathbf{J}(\mathbf{k} - \mathbf{k}_0) \quad (\text{A.1})$$

with

$$\mathbf{k} = \begin{Bmatrix} k_n \\ k_t \end{Bmatrix} \quad (\text{A.2})$$

and

$$\mathbf{J} = \begin{bmatrix} \frac{\partial f_{n,1B}}{\partial k_n} & \frac{\partial f_{n,1B}}{\partial k_t} \\ \frac{\partial f_{n,2B}}{\partial k_n} & \frac{\partial f_{n,2B}}{\partial k_t} \end{bmatrix} \quad (\text{A.3})$$

Vector \mathbf{k}_0 contains a pair of trial solutions and \mathbf{f}_0 its corresponding frequencies. The uncertainties $\delta f_{n,1B}$ and $\delta f_{n,2B}$ on the frequencies for the first and second bending mode were obtained from the the uncertainty on the measured axial load F_{ax} due to pressure gauge accuracy ($\delta p/p = \delta F_{ax}/F_{ax} = 1\%$).

$$\delta f_n = \frac{\partial f_n}{\partial F_{ax}} \delta F_{ax} \quad (\text{A.4})$$

F_{ax}	$\delta f_{n,1B}^m$	$\delta f_{n,2B}^m$
kN	Hz	Hz
12	0.23	0.40
14	0.25	0.45
16	0.29	0.50
18	0.33	0.55
20	0.33	0.54
22	0.35	0.55

Table A.2: measured natural frequencies uncertainties due to uncertainties on measured axial load F_{ax}

Sensitivity of the natural frequency f_n on axial load F_{ax} was estimated by using the FE model with the identified contact stiffnesses k_n and k_t . The

frequency covariance matrix is

$$\boldsymbol{\sigma}^2 := \langle \delta \mathbf{f} \delta \mathbf{f}^T \rangle = \begin{bmatrix} \sigma_{1B}^2 & 0 \\ 0 & \sigma_{2B}^2 \end{bmatrix} = \begin{bmatrix} \delta f_{n,1B}^2 & 0 \\ 0 & \delta f_{n,2B}^2 \end{bmatrix} \quad (\text{A.5})$$

with $\langle \cdot \rangle$ the expected value. In Eq. A.5 the standard deviations σ_{1B} and σ_{2B} are approximated with the uncertainties $\delta f_{n,1B}$ and $\delta f_{n,2B}$. Thus, the covariance matrix of contact stiffness at \mathbf{k}_0 is

$$\boldsymbol{\sigma}_{\mathbf{k}}^2 = \begin{bmatrix} \sigma_{nn}^2 & \sigma_{nt}^2 \\ \sigma_{tn}^2 & \sigma_{tt}^2 \end{bmatrix} = \langle \delta \mathbf{k} \delta \mathbf{k}^T \rangle = \mathbf{J}^{-1} \langle \delta \mathbf{f} \delta \mathbf{f}^T \rangle (\mathbf{J}^{-1})^T = \mathbf{J}^{-1} \boldsymbol{\sigma}^2 (\mathbf{J}^{-1})^T \quad (\text{A.6})$$

with $\delta \mathbf{f} = \mathbf{J} \delta \mathbf{k}$. The solution (named as optimal stiffness pair) was selected as the stiffness pair - on the minima locus - with the minimum 2norm of the stiffness covariance matrix. Standard deviations of k_n and k_t were computed from the covariance matrix

$$\mathbf{k}^{opt} = \left\{ \begin{array}{l} k_n^{opt} \\ k_t^{opt} \end{array} \right\} : \quad \min \|\boldsymbol{\sigma}_{\mathbf{k}}^2\|_2 \Rightarrow \left\{ \begin{array}{l} k_n = k_n^{opt} \pm \sigma_{nn} \\ k_t = k_t^{opt} \pm \sigma_{tt} \end{array} \right. \quad (\text{A.7})$$

References

- [1] M. Lavella, D. Botto, Fretting fatigue analysis of additively manufactured blade root made of intermetallic Ti-48Al-2Cr-2Nb alloy at high temperature, *Materials* 11 (2018) 1052. doi:10.3390/ma11071052.
- [2] M. Lavella, D. Botto, Fretting wear of alloy steels at the blade tip of steam turbines, *Wear* 426-427 (2019) 735-740. doi:10.1016/j.wear.2019.01.039.
- [3] M. Nakhla, J. Vlach, A piecewise harmonic balance technique for determination of periodic response of nonlinear systems, *IEEE Trans. Circuits Syst.* 23 (1976) 85-91. doi:10.1109/tcs.1976.1084181.
- [4] K. Sanliturk, D. Ewins, Modelling two-dimensional friction contact and its application using harmonic balance method, *J. Sound Vibr.* 193 (1996) 511-523. doi:10.1006/jsvi.1996.0299.

- 1
2
3
4
5
6
7
8
9 [5] C. Pierre, A. A. Ferri, E. H. Dowell, Multi-harmonic analysis of dry friction
10 damped systems using an incremental harmonic balance method, *J. Appl.*
11 *Mech.* 52 (1985) 958–964. doi:10.1115/1.3169175.
12
13
14 [6] A. Cardona, A. Lerusse, M. Géradin, Fast fourier nonlinear vibration anal-
15 475 ysis, *Comput. Mech.* 22 (1998) 128–142. doi:10.1007/s004660050347.
16
17
18 [7] C. Siewert, L. Panning, J. Wallaschek, C. Richter, Multiharmonic forced
19 response analysis of a turbine blading coupled by nonlinear contact forces,
20 *J. Eng. Gas. Turbines Power-Trans. ASME* 132 (2010). doi:10.1115/1.
21 4000266.
22
23
24
25 480 [8] E. P. Petrov, D. J. Ewins, Analytical formulation of friction interface
26 elements for analysis of nonlinear multi-harmonic vibrations of bladed disks,
27 *J. Turbomach.-Trans. ASME* 125 (2003) 364–371. doi:10.1115/1.1539868.
28
29
30 [9] S. Zucca, C. M. Firrone, M. M. Gola, Numerical assessment of friction
31 damping at turbine blade root joints by simultaneous calculation of the
32 static and dynamic contact loads, *Nonlinear Dyn.* 67 (2011) 1943–1955.
33 485 doi:10.1007/s11071-011-0119-y.
34
35
36
37 [10] S. Zucca, C. M. Firrone, Nonlinear dynamics of mechanical systems
38 with friction contacts: Coupled static and dynamic multi-harmonic bal-
39 ance method and multiple solutions, *J. Sound Vibr.* 333 (2014) 916–926.
40 490 doi:10.1016/j.jsv.2013.09.032.
41
42
43
44 [11] C. Gastaldi, T. Berruti, Competitive time marching solution methods
45 for systems with friction-induced nonlinearities, *Appl. Sci.* 8 (2018) 291.
46 doi:10.3390/app8020291.
47
48
49 [12] J. H. Griffin, Friction damping of resonant stresses in gas turbine engine
50 airfoils, *J. Eng. Gas. Turbines Power-Trans. ASME* 102 (1980) 329–333.
51 495 doi:10.1115/1.3230256.
52
53
54
55
56
57
58
59
60
61
62
63
64
65

- 1
2
3
4
5
6
7
8
9 [13] C. Menq, B. Yang, Non-linear spring resistance and friction damping of
10 frictional constraint having two-dimensional motion, *J. Sound Vibr.* 217
11 (1998) 127–143. doi:10.1006/jsvi.1998.1739.
12
13
14 500 [14] B. Yang, C. Menq, Characterization of 3d contact kinematics and predic-
15 tion of resonant response of structures having 3d frictional constraint, *J.*
16 *Sound Vibr.* 217 (1998) 909–925. doi:10.1006/jsvi.1998.1802.
17
18
19 [15] B. Yang, M. Chu, C. Menq, Stick-slip-separation analysis and non-linear
20 stiffness and damping characterization of friction contacts having variable
21 normal load, *J. Sound Vibr.* 210 (1998) 461–481. doi:10.1006/jsvi.1997.
22 505 1305.
23
24
25 [16] K. L. Johnson, Surface interaction between elastically loaded bodies under
26 tangential forces, *Proc. R. Soc. Lond. A* 230 (1955) 531–548. doi:10.1098/
27 *rspa.1955.0149*.
28
29
30 510 [17] B. N. Norden, On the compression of a cylinder in contact with a plane
31 surface, Technical Report, 1973. doi:10.6028/nbs.ir.73-243.
32
33
34 [18] R. Roark, Formulas for stress and strain, McGraw-Hill, New York, 1975.
35
36
37 [19] J. Brandlein, P. Eschmann, L. Hasbargen, K. Weigand, Ball Roller Bear-
38 ings, Third edition, John Wiley & Sons, 1999.
39
40
41 515 [20] O. I. Kosarev, Contact deformation and compression of cylinders, *Russ.*
42 *Eng. Res.* 31 (2011) 107–112. doi:10.3103/s1068798x11020122.
43
44
45 [21] C. Cattaneo, Sul contatto di due corpi elastici, *Accademia dei Lincei,*
46 *Rendiconti, Serie 6, foglio 27* (1938) 342–348, 434–436, 474–478.
47
48
49 [22] R. D. Mindlin, Compliance of elastic bodies in contact, *J. Appl. Mech.* 16
50 51 (1949) 259–268.
52 520
53
54 [23] H. Deresiewicz, Oblique contact of nonspherical elastic bodies, *J. Appl.*
55 *Mech.* 24 (1957) 623–624.
56
57
58
59
60
61
62
63
64
65

- 1
2
3
4
5
6
7
8
9 [24] I. Shtayerman, Contact Problem of the Theory of Elasticity, Translation
10 Division, Foreign Technology Division, 1970.
11
- 12
13 525 [25] M. Ciavarella, D. A. Hills, G. Monno, The influence of rounded edges on
14 indentation by a flat punch, Proc. Inst. Mech. Eng. Part C-J. Eng. Mech.
15 Eng. Sci. 212 (1998) 319–327. doi:10.1243/0954406981521259.
16
17
- 18 [26] M. Allara, A model for the characterization of friction contacts in turbine
19 blades, J. Sound Vibr. 320 (2009) 527–544. doi:10.1016/j.jsv.2008.08.
20
21 530 016.
22
- 23 [27] M. Umer, D. Botto, Measurement of contact parameters on under-platform
24 dampers coupled with blade dynamics, Int. J. Mech. Sci. 159 (2019) 450–
25 458. doi:10.1016/j.ijmecsci.2019.06.010.
26
27
- 28 [28] J. Chen, C. Zang, B. Zhou, E. Petrov, High-fidelity calculation of modal
29 damping caused by friction at blade roots for single blades and tuned bladed
30 disc assemblies, Proc. Inst. Mech. Eng. Part C-J. Eng. Mech. Eng. Sci.
31 535 (2020) 095440622093514. doi:10.1177/0954406220935144.
32
33
- 34 [29] J. Chen, C. Zang, B. Zhou, E. P. Petrov, Analysis of nonlinear modal
35 damping due to friction at blade roots in mistuned bladed disks, J. Eng.
36 Gas. Turbines Power-Trans. ASME 143 (2021). doi:10.1115/1.4049860.
37
38 540
39
40
- 41 [30] R. D. Mindlin, W. P. Mason, T. F. Osmert, H. Deresiewicz, Effects of an
42 oscillating tangential force on the contact surfaces of elastic spheres, in:
43 Proc. 1st Nat. Congr. Appl. Mech., 1952, pp. 203 – 208.
44
45
- 46 [31] L. E. Goodman, C. B. Brown, Energy dissipation in contact friction: Con-
47 stant normal and cyclic tangential loading, J. Appl. Mech. 29 (1962) 17–22.
48 545
49
50
51
52
53
54
55
56
57
58
59
60
61
62
63
64
65

- 1
2
3
4
5
6
7
8
9
10
11
12
13
14
15
16
17
18
19
20
21
22
23
24
25
26
27
28
29
30
31
32
33
34
35
36
37
38
39
40
41
42
43
44
45
46
47
48
49
50
51
52
53
54
55
56
57
58
59
60
61
62
63
64
65
- 550 [33] S. Filippi, E. B. Rodrigues, M. M. Gola, Experimental characterization of contact hysteresis at high temperatures, volume Volume 5: Marine; Micro-turbines and Small Turbomachinery; Oil and Gas Applications; Structures and Dynamics, Parts A and B of *Turbo Expo: Power for Land, Sea, and Air*, 2006, pp. 893–902. doi:10.1115/gt2006-90757.
- 555 [34] D. Botto, M. Lavella, High temperature tribological study of cobalt-based coatings reinforced with different percentages of alumina, *Wear* 318 (2014) 89–97. doi:10.1016/j.wear.2014.06.024.
- [35] A. B. Stanbridge, D. J. Ewins, K. Y. Sanliturk, J. V. Ferreira, Experimental investigation of dry friction damping and cubic stiffness non-linearity, volume Volume 6B: 18th Biennial Conference on Mechanical Vibration and Noise of *International Design Engineering Technical Conferences and Computers and Information in Engineering Conference*, 2001, pp. 2141–2148. doi:10.1115/detc2001/vib-21556.
- 560 [36] C. Schwingshackl, E. Petrov, D. Ewins, Measured and estimated friction interface parameters in a nonlinear dynamic analysis, *Mech. Syst. Signal Proc.* 28 (2012) 574–584. doi:10.1016/j.ymsp.2011.10.005.
- [37] M. Lavella, D. Botto, M. M. Gola, Test rig for wear and contact parameters extraction for flat-on-flat contact surfaces, volume ASME/STLE 2011 Joint Tribology Conference of *International Joint Tribology Conference*, 2011, pp. 307–309. doi:10.1115/ijtc2011-61234.
- 570 [38] D. Li, D. Botto, C. Xu, M. Gola, A new approach for the determination of the iwan density function in modeling friction contact, *Int. J. Mech. Sci.* 180 (2020) 105671. doi:10.1016/j.ijmecsci.2020.105671.
- [39] D. Li, D. Botto, C. Xu, T. Liu, M. Gola, A micro-slip friction modeling approach and its application in underplatform damper kinematics, *Int. J. Mech. Sci.* 161-162 (2019) 105029. doi:10.1016/j.ijmecsci.2019.105029.

- 1
2
3
4
5
6
7
8
9 [40] D. Li, C. Xu, D. Botto, Z. Zhang, M. Gola, A fretting test apparatus
10 for measuring friction hysteresis of bolted joints, *Tribol. Int.* 151 (2020)
11 106431. doi:10.1016/j.triboint.2020.106431.
12
13
14 580 [41] M. Umer, C. Gastaldi, D. Botto, Friction damping and forced-response of
15 vibrating structures: An insight into model validation, *Int. J. Solids Struct.*
16 202 (2020) 521–531. doi:10.1016/j.ijsolstr.2020.07.002.
17
18
19 [42] M. Allara, S. Filippi, M. M. Gola, An experimental method for the mea-
20 surement of blade-root damping, volume Volume 5: Marine; Microturbines
21 and Small Turbomachinery; Oil and Gas Applications; Structures and Dy-
22 namics, Parts A and B of *Turbo Expo: Power for Land, Sea, and Air*, 2006,
23 585 pp. 903–912. doi:10.1115/gt2006-90774.
24
25
26 [43] D. Botto, F. Cuccovillo, V. Iannotti, Experimental investigation of friction
27 damping in blade root joints, *Journal of Engineering for Gas Turbines and*
28
29
30
31 590 *Power* 145 (2022). doi:10.1115/1.4056099.
32
33
34 [44] C. M. Firrone, I. Bertino, Experimental investigation on the damping
35 effectiveness of blade root joints, *Exp. Mech.* 55 (2015) 981–988. doi:10.
36 1007/s11340-015-0001-9.
37
38
39 [45] F. J. Marquina, A. Coro, A. Gutie´rrez, R. Alonso, D. J. Ewins, G. Girini,
40
41 595 Friction damping modeling in high stress contact areas using microslip
42 friction model, volume Volume 5: Structures and Dynamics, Parts A and
43 B of *Turbo Expo: Power for Land, Sea, and Air*, 2008, pp. 309–318. doi:10.
44 1115/gt2008-50359.
45
46
47 [46] K. Asai, S. Sakurai, T. Kudo, N. Ozawa, T. Ikeda, Evaluation of friction
48
49 600 damping in dovetail root joints based on dissipation energy on contact sur-
50 faces, volume Volume 6: Structures and Dynamics, Parts A and B of *Turbo*
51 *Expo: Power for Land, Sea, and Air*, 2009. doi:10.1115/gt2009-59508.
52
53
54 [47] H. R. Simmons, V. Iyengar, Effect of non-uniform blade root friction and
55 sticking on disk stresses, volume Volume 6: Structures and Dynamics,
56
57
58

1
2
3
4
5
6
7
8
9
10
11
12
13
14
15
16
17
18
19
20
21
22
23
24
25
26
27
28
29
30
31
32
33
34
35
36
37
38
39
40
41
42
43
44
45
46
47
48
49
50
51
52
53
54
55
56
57
58
59
60
61
62
63
64
65

605 Parts A and B of *Turbo Expo: Power for Land, Sea, and Air*, 2011, pp. 829–838. doi:10.1115/gt2011-46689.

[48] M. Feldman, Non-linear system vibration analysis using hilbert transform–i. free vibration analysis method 'freevib', *Mech. Syst. Signal Proc.* 8 (1994) 119–127. doi:10.1006/mssp.1994.1011.

610 [49] M. Feldman, *Hilbert Transform Applications in Mechanical Vibration*, John Wiley & Sons, Ltd, 2011. doi:10.1002/9781119991656.

[50] R. E. Ziemer, W. H. Tranter, *Principles of Communication. Systems, Modulation, and Noise*, 7th edition, John Wiley & Sons, 2014.

[51] A. Bokaian, Natural frequencies of beams under tensile axial loads, *J. Sound Vibr.* 142 (1990) 481–498. doi:10.1016/0022-460x(90)90663-k.

615 [52] R. R. Craig, M. C. C. Bampton, Coupling of substructures for dynamic analyses., *AIAA J.* 6 (1968) 1313–1319. doi:10.2514/3.4741.

[53] A. E. H. Love, *A Treatise on the Mathematical Theory of Elasticity*, Cambridge University Press, 1892.

620 [54] G. Starzynski, R. Buczkowski, Ultrasonic measurements of contact stiffness between rough surfaces, *J. Tribol.-Trans. ASME* 136 (2014). doi:10.1115/1.4027132.

[55] H. Andresen, D. Hills, J. Barber, J. Vázquez, Steady state cyclic behaviour of a half-plane contact in partial slip subject to varying normal load, moment, shear load, and moderate differential bulk tension, *Int. J. Solids Struct.* 182-183 (2020) 156–161. doi:10.1016/j.ijsolstr.2019.07.027.

625 [56] P. H. Richter, *Estimating Errors in Least-Squares Fitting*, techreport 42-122, NASA, 1995.